J Mater Sci: Mater Electron (2023)34:438

Effect of Mn doping on structural, optical and magnetic properties of ZnO films fabricated by sol–gel spin coating method

Zafer Gültekin[1], Mürsel Alper[1,*], M. Cüneyt Hacıismailoğlu[1], and Cengiz Akay[1]

[1] *Department of Physics, Science and Art Faculty, Bursa Uludag University, 16059 Görükle, Bursa, Turkey*

Received: 25 September 2022
Accepted: 11 January 2023

© The Author(s), under exclusive licence to Springer Science+Business Media, LLC, part of Springer Nature 2023

ABSTRACT

We have fabricated undoped ZnO and Mn-doped ZnO thin films on glass substrates using sol–gel spin coating method and investigated their structural, optical, magnetic and magnetoresistance properties depending on the Mn doping ratio. X-ray diffraction (XRD) patterns showed that all the films under study are predominantly crystalized in a single-phase wurtzite structure. Scanning electron microscope (SEM) images revealed that the films become more homogeneous, continuous and pinhole-free coatings as the Mn content of the films increases. Optical characterizations by UV–visible spectrometer indicated that transmittance spectra of all films have a high transmittance above 85% in visible region, while they show the absorbance spectra in 300–400 nm range. In addition, it was observed that the optical energy band edges shift to red with increasing Mn content, due to probably increasing the carrier concentration. The refractive index and the dielectric constant are also affect by the Mn content. Magnetic measurements by vibrating sample magnetometer showed that the film magnetic properties change from diamagnetic to ferromagnetic as the Mn content increases. Furthermore, it was found that the magnetoresistance measurements support their magnetic behavior of the films.

1 Introduction

In recent years, transparent conducting oxide (TCO) films have been the subject of intensive studies since they have wide applications in optoelectronic devices. The most popular material in TCOs is tin-doped indium oxide (ITO) which is used in commercials due to its high conductivity, work function and transparency in the visible spectral range. However, although ITO films are probably the most useful TCOs, they have some disadvantages such as the scare of indium in the earth's crust, high cost and chemical instability. So, in order to find appropriate alternative materials to ITO, the studies have been focused on several metal oxides such as undoped and doped CdO [1, 2], ZnO [3–6] and SnO_2 [7]. Among

Address correspondence to E-mail: malper@uludag.edu.tr

https://doi.org/10.1007/s10854-023-09886-7
Published online: 04 February 2023

them, one of the most remarkable metal oxides is zinc oxide (ZnO), which is an n-type semiconductor having a direct band gap of 3.37 and a large exciton binding energy of 60 meV, high transparency, high electron mobility, and high stability and biocompatibility at room temperature [8–10]. Furthermore, ZnO is a promising candidate material that can be used as functional components in many devices such as varistors, biosensors, piezoelectric devices, gas sensors, solar cells, organic light-emitting diodes (OLED) [11–13]. By adding different elements such as Al, Sn, Cu, Co, Mn and Fe into ZnO, its properties such as the band gap, electrical conductivity, the carrier concentration and magnetic can be manipulated for various applications [14–17].

In particular, when ZnO is doped by transition metals (Mn, Cr, Co, Ni, Fe), it may exhibit the ferromagnetic property. Thus, the semiconductor metal oxides having the ferromagnetic effect are called as dilute magnetic semiconductors (DMS). In DMSs, the substitution of non-magnetic component Zn ion by a 3d transition metal ion within ZnO crystal lattice leads to the ferromagnetic behavior while retaining semiconducting properties as well [18]. Therefore, DMSs have great potential applications in spintronics device such as optoelectronics, sensors, spin-valve transistors, spin light-emitting diodes, non-volatile memory. Generally, in order to gain the ferromagnetic property, ZnO nanomaterials are doped by Co, Mn and CoMn, because the ionic radius of Co and Mn is close to that of Zn and hence they are easily incorporated into the ZnO lattice [14, 19]. It was also reported that a significant transition from the diamagnetic state for undoped ZnO to the ferromagnetic state for doped (Co, Mn, Fe) ZnO, depends on the magnetic impurity concentration. This ferromagnetism effect observed Mn- and Co-doped ZnO films has attracted the interesting of the researchers from both scientific and technological application point of view. In order to explain the mechanism and origin of the magnetic properties of DMSs based on ZnO, although several theoretical and experimental studies have been made by different methods and groups, there is no clear agreement between them [18, 20, 21]. So, the ferromagnetism effect still continues to be the subject of an extensive discussion related to its mechanism.

Today there are several methods to synthesize doped or undoped ZnO films, such as chemical vapor deposition, electron beam evaporation, sputtering, molecular beam epitaxy, pulsed laser deposition, spray pyrolysis and sol–gel spin coating [22–26]. The sol–gel spin coating technique is one of the easiest ways to produce ZnO films on different substrates and also offers many advantages compared to other techniques such as excellent homogeneity, low cost, thickness control and the possibility of coating vast and complex surfaces and low-temperature processing [27, 28].

When designing an optoelectronic device, like OLED, in order to be able to adjust the efficiency of the device, it is necessary to know the structural, electrical and optical properties of the layers that make up the structure. In particular, it is important to consider the refractive index as a function of wavelength to predict the photoelectric behavior of a device [29]. Also, regarding the encapsulants for organic light-emitting diodes (OLEDs), commercial applications require materials with high refractive index, low birefringence, high optical transparency and long-term ultraviolet light and thermal stability [30].

In this study, undoped ZnO and ZnO films having different Mn doping ratios were fabricated using a homemade sol–gel spin coating technique with our own software. The detail of the experimental technique was published elsewhere [31]. Although the structural, optical and electrical properties of undoped and Mn–ZnO thin films have been extensively studied [9, 14], there are very limited reports on their magnetic and magnetoresistance properties, which are important parameters for spintronic devices such as spin-OLED. Furthermore, the mechanism behind the magnetic ordering in doped ZnO films is still under debate. Therefore, we have investigated the structural, optical, magnetic and magnetoresistance (MR) properties of the films depending on the Mn content and also the relationship between their room temperature (RT) ferromagnetism (FM) and MR. To our knowledge, the room temperature MR behavior is the first observation for Mn-doped ZnO films fabricated by the sol–gel spin coating technique. We have also demonstrated that the film properties significantly vary with their Mn content and especially there is a relation between magnetic and MR behaviors.

2 Experimental

In order to synthesis ZnO films, $Zn(CH_3CO_2)_2{\cdot}2H_2O$ (zinc acetate dihydrate), methoxyethanol as solvent and monoethanolamine (MEA) as a stabilizer were

used. Firstly, zinc acetate dihydrate of 4.40 g was dissolved in methoxyethanol of 40 ml at 60 °C (centigrade degrees) and at 800 rpm stirring speed for 10 min. Then, to this mixture, MEA of 1.22 g was added dropwise and mixed for 2 h at 60 °C. For the synthesis of Mn–ZnO, $(CH_3COO)_2Mn{\cdot}4H_2O$ (manganese (II) acetate tetrahydrate) was added in different molar ratios (0.1, 0.2 and 0.3 M) into and mixed for 15 min. After all solutions were aged for 1 day at room temperature, ZnO and Mn–ZnO films were deposited on glass substrates using sol–gel spin coating technique. The substrates were cleaned with standard cleaning procedures and then kept in 30% HCl (hydrochloric acid) solution for 2 h to obtain extra clean surfaces. The deposition process was carried out at a spin speed of 3000 rpm and a time of 60 s. To remove solvent and inorganic residues from the deposits, they were dried in an oven preheated to 150 °C for 30 min.

The structural characterizations of the samples were studied by Bruker AXS/Discovery D8 X-ray diffractometer with Cu K_α (λ = 0.15406 nm) radiation for the diffraction angles 2θ ranging between 30 and 100°. The surface morphology of the films was examined by scanning electron microscope (SEM) (Carl Zeiss/Gemini 300). The elemental composition was determined by X-ray energy-dispersive spectrometer (EDX) equipped with SEM. The optical properties were examined by using UV–Vis spectrophotometer (Flame, Ocean Optics) operated in both absorption and transmittance mode. The measurements were taken at the wavelengths ranged from 300 to 800 nm with a resolution of 1 nm at the room temperature.

The magnetic and magnetoresistance measurements were taken at room temperature by vibrating sample magnetometer (VSM, Microsense-EZ9) in the magnetic fields varied between ± 20 kOe, which were applied parallel to the plane of the thin films. Magnetoresistance (MR) measurements were taken using the Van der Pauw technique with a sample holder of square shaped with four probes on its corner. The magnetic fields (H) were applied approximately parallel and perpendicular to the direction of the current (I) flowing in the film plane to measure the longitudinal and transverse magnetoresistance, respectively, as described in previous work [31, 32]. In each case, the percentage change in the resistance MR(%) as a function of the applied magnetic field was calculated by the relation $MR(\%)=\{[R(H) - R_{min}]/R_{min}\} \times 100$, where $R(H)$ is the value of the resistance at any magnetic field and R_{min} is the value at the field where the resistance is minimum.

3 Results and discussion

3.1 Structural characterizations

The X-ray diffraction patterns of undoped and Mn–ZnO thin films are shown in Fig. 1 as well as glass substrate. As seen from the figure, although the substrate is amorphous structure, all the films have almost sharp and narrow diffraction peaks, indicating that the films exhibit high crystallinity. The XRD patterns confirmed that all the films are polycrystalline and predominantly exhibit hexagonal wurtzite structure of ZnO. The diffraction peaks appeared at the diffraction angles of about 31.6, 33.5, 36.4, 48.4, 57.4 and 61.1 degrees belong to (100), (002), (101), (102), (110) and (103) planes of the ZnO structure, respectively. The observed patterns are in good agreement with JCPDS card No. 36-1451 [33] and the reported results [15, 27]. Three main peaks from (100), (002) and (101) planes of the wurtzite structure are stronger than other peaks. After Mn doping, the main peaks belonging to (100), (002) and (101) planes occur at about the same diffraction angles again, as in undoped ZnO, while the peak from (002) shifts slightly to the smaller angle and (110) peak to the

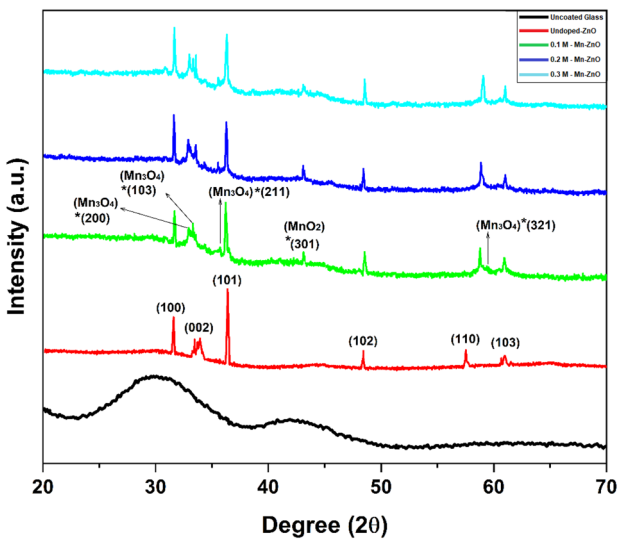


Fig. 1 X-ray diffraction patterns of undoped and Mn–ZnO thin films

larger angle compared to undoped ZnO. Such changes can be expected because some Mn ions replace Zn ions in the crystal lattice, as the radius of Mn ions (Mn^{+4}: 0.056 nm, and Mn^{+3}: 0.062 nm) is smaller than that of Zn (0.074 nm). The shift in the position of some peaks to higher/lower angles with the Mn dopant may arise from the compression/expansion of the lattice parameters, respectively (see Table 1), due to the size difference between the Zn and Mn atoms. The peak broading may be considered as a result of the overlap of the adjacent peaks at about the same angular positions of some Mn oxides and ZnO. Furthermore, in all the films with Mn doped, the peaks coming from MnO_2 and Mn_3O_4 were detected. These were labelled in XRD patterns (in Fig. 1) and indexed [34–36], but these peaks appear as highly low intensities and hence Mn oxides can be considered as a weak secondary phase in the main compound. By calculating the area of each peak, the fraction of Mn oxides in the crystal structure was determined and found to be too much low. This means that Mn ions could have highly incorporated into the ZnO lattice and the Mn dopant seems not to be a considerable impact on the crystal structure of the ZnO samples. On the other hand, the reason of the change in the integrated intensities of some peaks is probably related to the fraction of the grains in a (hkl) orientation in the crystal structure of the samples.

Using the XRD data in Fig. 1, the lattice parameters calculated according to the Bragg law are listed in Table 1. As the Mn content increases, the parameter c increases slightly, while a is almost constant within the experimental errors. Average crystallite sizes of the samples were determined from the full width at half maximum (FWHM) of peaks in the XRD patterns using the Debye–Scherrer formula (1) [14]:

$$D = \frac{K\lambda}{\beta\cos\theta}, \quad (1)$$

where K is the shape factor (0.9), λ is the wavelength of the Cu K_α, β is the FWHM of the most intense peak of the XRD spectrum, and θ is the Bragg angle. According to the Mn concentration in the solution, the calculated crystallite sizes (D) and the determined Mn content from EDX data are given in Table 1. As expected, as the Mn concentration in the solution increases, the Mn content of the film increases. As seen from the table, all samples have nanometric grain size, which decreases with the increasing Mn content of the film. This decrease in the grain size may be due to the distortion produced by the foreign impurities in the host ZnO crystal structure. Our results agree with some reported studies [37].

Figure 2 shows the SEM images of undoped ZnO and Mn–ZnO films as well as their cross-section pictures in the insets. In Fig. 2a, for undoped ZnO films, the surface is homogeneously coated by ZnO and has a uniform grain size distribution and the mean grain size is about 55 nm, which is in agreement well with the value (58 nm) found from the XRD data. Figure 2 b, c and d shows the surface pictures of Mn–ZnO thin films produced from the solutions containing 0.1, 0.2 and 0.3 M Mn, respectively. As seen from the figure, Mn–ZnO films have similar surface morphology that becomes more homogeneous and smooth compared to the surface of undoped ZnO film, which is associated with a decrease in the crystallite size with increasing Mn dopant. From the cross-section images in the insets, the thicknesses of samples were determined for undoped and Mn-doped ZnO films and are given in Table 1. Note that the thickness of the Mn-doped films (600 to 650 nm) is smaller than that of undoped ZnO (700 nm). These discrepancies in the surface morphology and thicknesses can be explained by the differences in the ionic radius of Zn and Mn ions. The Mn ions with smaller radius than Zn ions can place in spaces between ZnO nanoparticles. Thus the Mn

Table 1 Results calculated from XRD, SEM and EDX data

Mn concentration in solution (M)	Mn content in Mn–ZnO films (EDX)	Lattice parameters		Crystal size D (nm) (XRD)	Thickness (nm) (SEM)
		$a = b$ (nm)	c (nm)		
Undoped—ZnO	NA	0.328	0.501	58	700
0.1 M—Mn–ZnO	6.09	0.327	0.513	55	625
0.2 M—Mn–ZnO	10.02	0.328	0.513	51	600
0.3 M—Mn–ZnO	13.19	0.327	0.507	46	650

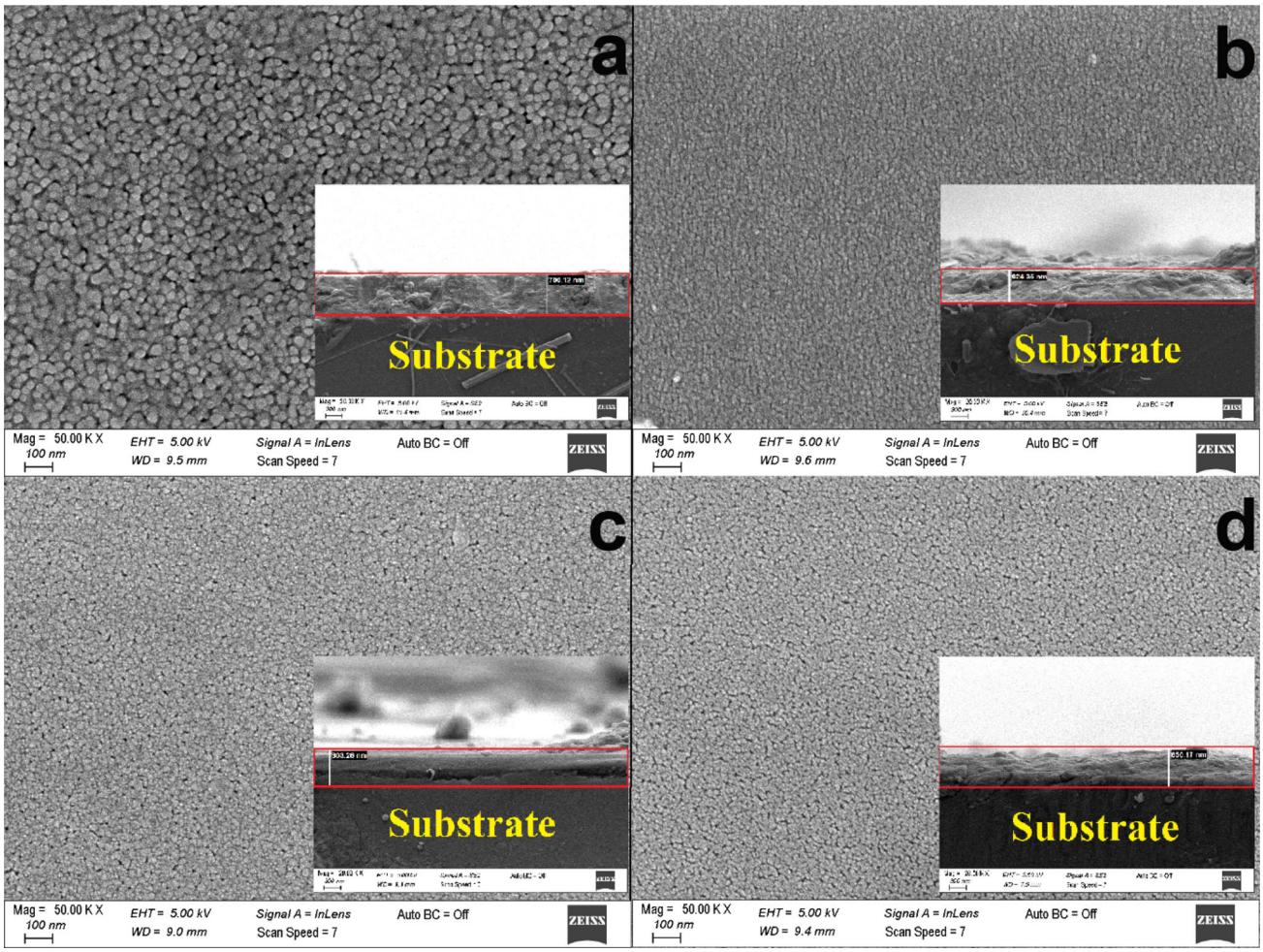


Fig. 2 SEM images of **a** undoped, **b** 0.1 M, **c** 0.2 M, **d** 0.3 M, Mn–ZnO thin films. The insets are cross sections of undoped ZnO and Mn–ZnO

doping may increase the disorder in the ZnO films, which also affect its crystallinity [37].

Figure 3a shows the recorded EDX spectrum for undoped ZnO thin films. The presence of Zn and O in the studied energy range confirms the formation of ZnO thin films, which contains 44.95 wt% Zn and 55.05 wt% O. The EDX spectra for Mn–ZnO thin films obtained for three different Mn concentration values are shown in Fig. 3b–d. The EDX spectra detected the incorporation of Mn into the crystal structure of ZnO films. The presence of Mn in addition to Zn and O in the investigated energy range indicates the formation of Mn–ZnO thin films. The Mn content of the films prepared from the solutions of 0.1, 0.2 and 0.3 M concentrations was determined to be 6.09 wt%, 10.02 wt% and 13.19 wt%, respectively, which are also available in Table 1.

3.2 Optical properties

The optical properties of metal oxide films are affected by several factors such as nature, substrate, crystallinity, the film thickness and the amount of dopants. These factors also influence the electrical properties of the films. In order to investigate the optical properties of the films, the absorbance and transmittance measurements were taken in the wavelength range of 300–800 nm by UV–Visible Light Spectrometer (Ocean Optics). Figure 4a and b shows the transmittance and absorbance spectra of undoped and Mn–ZnO thin films, according to the Mn content. As seen from Fig. 4b, the transmitting edge for all the films increases rapidly in the wavelength range of 300–400 nm and then reaches the transmittance values of about 80–90% in the visible region. As the Mn content of the film increases, the

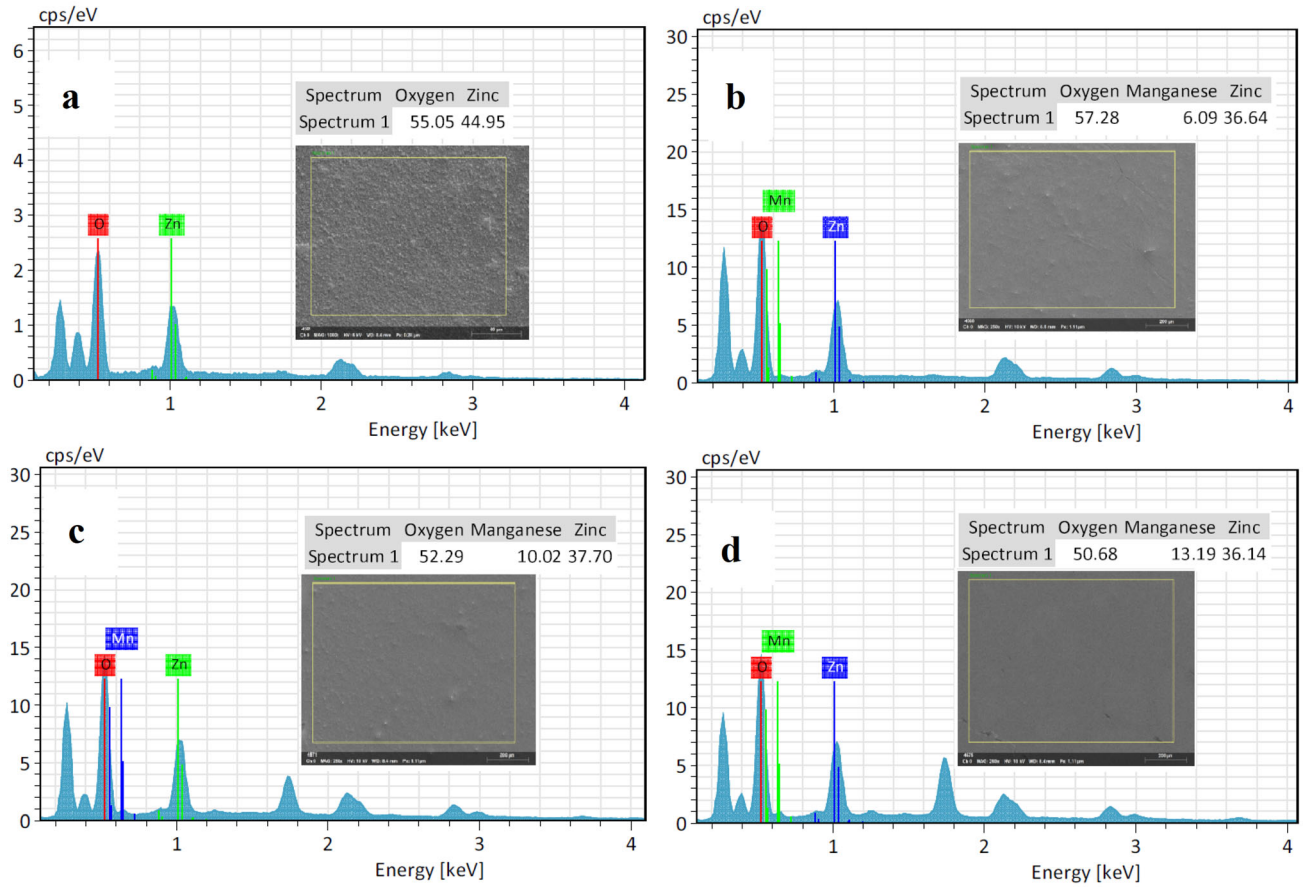


Fig. 3 EDX spectra of **a** undoped, **b** 0.1 M, **c** 0.2 M and **d** 0.3 M, Mn–ZnO thin films. The elemental composition shows the percentage weighted (wt%) ratios for Zn, O and Mn in the films

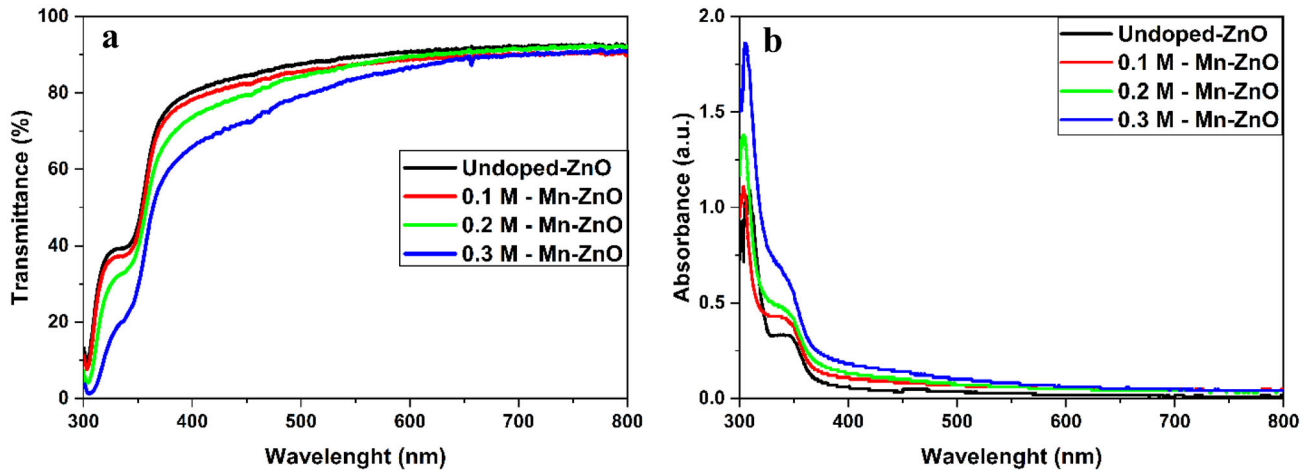


Fig. 4 Transmittance (**a**) and **b** absorbance spectra of undoped ZnO and Mn-doped ZnO thin films

transmittance values decrease. The optical transmittance is closely related to the doping concentration, which is associated with the carrier concentration in Mn-doped ZnO films (Table 1). The decrease in the transmittance with Mn doping concentration may be due to the increased scattering of photons by crystal defects (oxygen vacancy and grain boundaries) causing to the doping, difference in thickness and the

surface roughness of the samples. The addition of Mn ions into Zn^{2+} sol solution increases the number of nucleation sites, resulting in higher grain boundary density [38]. In turn, this increases the scattering of light and hence reduces the optical transmittance of the films [39–41].

As light passes through a material, it is absorbed to an extent depending on the nature of substance and its thickness. The absorbance of the material is inversely related to its transmittance. Figure 4b shows the absorbance spectrum of undoped and Mn–ZnO thin films. Especially in the UV region 300–400 nm, the absorbance changes significantly with the Mn content. In this region, all samples have a varying ultraviolet absorption edge. Beyond this point, the absorbance remains almost constant. As the Mn doping concentration increases, contrary to the transmittance, the absorbance increases, compared to the undoped ZnO, and the absorbance edge shifts to red. This is attributed to the changes in the morphology, particle sizes and band gaps of the films [42, 43] and also is thought to be from more photon absorption because of the introduction of Mn defects into the forbidden band [44].

The absorbance coefficient (α) is defined as a measure of the change in energy as the light passes through the film and it determines how far the light with a particular wavelength can penetrate into the material before absorbing and is calculated according to Eq. (2) [45]:

$$\alpha = \frac{(2.303xA)}{t}, \tag{2}$$

where t is the film thickness and A is the absorbance. The α values calculated for a wavelength of 600 nm are listed in Table 2. Figure 5a shows the variation of the absorption coefficients (α) for undoped ZnO and Mn–ZnO thin films with the wavelength. As expected, the absorption coefficient increases with increasing the Mn content, which is consistent with the corresponding absorbance in Fig. 4b.

In order to better understand the optical properties of the films are required to study some parameters, which are the extinction coefficient and the refractive index. The extinction coefficient is defined a measure of the light lost per unit volume due to scattering and absorption, while the refractive index refers to the relative velocity of the passing through a material. The extinction coefficient (k) can be found by Eq. (3) [46]:

$$k = \frac{\alpha\lambda}{4\pi}, \tag{3}$$

where λ is wavelength. The k values calculated for a wavelength of 600 nm are given in Table 2. The change of the extinction coefficient with the wavelength is given in Fig. 5b for undoped ZnO and Mn–ZnO thin films. It is clearly seen that the extinction coefficient increases and a red shift was observed in the small wavelength ranges (> 400 nm) with the increase in Mn doping.

The fundamental absorption edge (E_g) of the films is in the wavelength range of 250–350 nm and can be attributed to a direct band gap, where the absorption coefficient (α) can be correlated to the optical band gap (E_g), as described in the Tauc equation (4) [47]:

$$\alpha h\upsilon = B(h\upsilon - E_g)^{1/2}, \tag{4}$$

where B is a constant of proportionality and $h\upsilon$ is the photon energy. This equation indicates a linear dependence of $(\alpha h\upsilon)^2$ on the photon energy ($h\upsilon$). The plots of $(\alpha h\upsilon)^2$ versus energy ($h\upsilon$) are shown in Fig. 6 for undoped ZnO and Mn–ZnO thin films. As seen clearly in the inset, the extrapolation to the energy axis of the straight line zone of $(\alpha h\upsilon)^2$ versus energy ($h\upsilon$) plots gives the E_g values for each sample (Table 2). As the Mn doping ratio increases, the optical band gap shifts to red (to lower energies) compared to that of undoped ZnO, that is, from 3.41 eV for undoped ZnO down to 3.35 eV for the Mn doping ratio of 0.3 M. This indicates that the Mn doping reduces the band gap of ZnO. This result is also confirmed by the increase in the carrier concentration with increasing Mn content and similar to that of MnO_2–ZnO nanomaterials [48]. It was reported that the presence of impurities in ZnO leads to the decrease in its energy band gap [49]. Thus, the decrease in the energy band gap facilitates the transition of the electron from the valence band to the conduction band. Therefore, it can be concluded that the electron flow becomes more in Mn–ZnO samples compared to undoped ZnO [50]. In addition, it was also reported that the decrease in band gap with increasing Mn content can be attributed to structural morphology, particle size and surface microstructure

Table 2 Optical parameters calculated at a wavelength of 600 nm from the optical data of undoped ZnO and Mn–ZnO thin films

Mn concentration in solution (M)	Carrier concentration ($\times 10^{18}$) cm^{-3}	Bandgap (eV)	Absorption coefficient (α)	Extinction coefficient (k)	Refractive index (n)	Dielectric constant	
						ε_r	ε_i
Undoped ZnO	1.93	3.41	0.00040	0.02	1.66	2.76	0.06
0.1 M—Mn–ZnO	2.02	3.39	0.00115	0.05	1.89	3.53	0.20
0.2 M—Mn–ZnO	2.10	3.38	0.00116	0.06	1.88	3.58	0.21
0.3 M—Mn–ZnO	2.35	3.35	0.00139	0.07	1.96	3.85	0.26

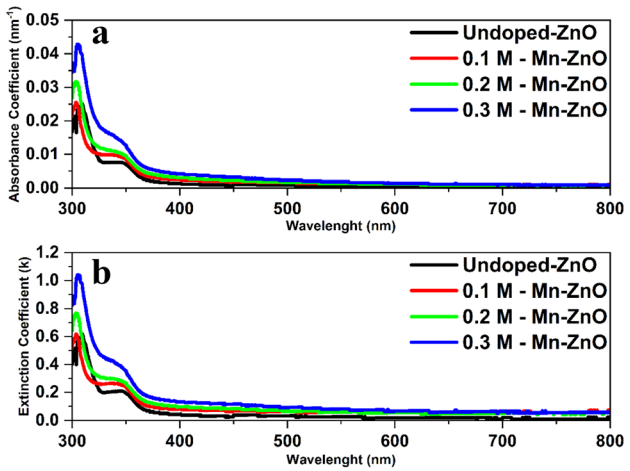


Fig. 5 The variation of the absorbance (**a**) and extinction (**b**) coefficients with the wavelength for undoped ZnO and Mn–ZnO thin films

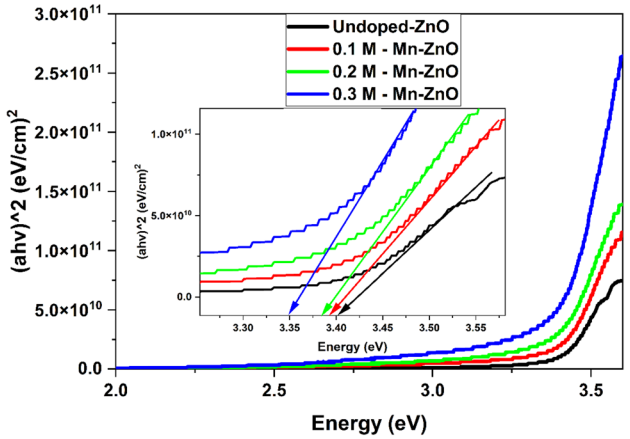


Fig. 6 Band gaps of undoped ZnO and Mn–ZnO thin films

[43] and s–d and p–d interactions leading to band gap bending [51, 52].

In order to obtain more information about the optical properties of the samples, their refractive indices were studied. The refractive index (n) was calculated using the relation [45, 53, 54] as follow:

$$R = \frac{(n-1)^2 + k^2}{(n+1)^2 + k^2}, \tag{5}$$

where k is the extinction coefficient, and R is reflectance and $R + A + T = 1$. The change of the refractive index with the wavelength is given in Fig. 7 for undoped ZnO and MnZnO thin films.

As seen clearly from the figure, as the Mn content increases, the refractive index increases compared to that of the undoped ZnO. This increase may be due to the fact that Mn is injected into the matrix in the host material (ZnO), forming atom clusters and increasing the impurities. In addition, the spectral behavior of the refractive index can be studied in two regions: First, the abnormal distribution region at $\lambda < 350$ nm where the refractive index shows high values and second, the normal distribution region at $\lambda \geq 350$ nm where the refractive index decreases rapidly and then remains almost constant. The most ideal refractive index value in the abnormal distribution region is obtained when the frequency of the incident photon is equal to the plasma frequency of the oscillating electric dipoles. In this region, the binding of electrons in thin films to the oscillating electric field occurs [55, 56]. The decrease in refractive index at normal region is due to a decrease in optical surface dispersion, polarizability and optical losses which may be due to reduction in surface roughness and enhancement in carrier concentration [57].

Figure 8a and b shows the real and imaginary parts of the optical dielectric constant of undoped ZnO and Mn–ZnO thin films, respectively. The real (ε_r) and imaginary (ε_i) parts of the optical dielectric constant were calculated using formulas (6) and (7) given in [23], respectively:

$$\varepsilon_r = n^2 - k^2, \tag{6}$$

$$\varepsilon_i = nk, \tag{7}$$

where n is the refractive index, and k is the extinction coefficient. The real part of the dielectric constant indicates how much the speed of light slows down in a material, while the imaginary part relates to the dielectric material, which absorbs energy from the electric field due to dipole motion. Both the real and imaginary parts of the dielectric constant increase with the increase in the Mn doping ratio. As seen from the figure, the real part values, which indicate the transparency of thin films, are higher than the virtual [58] and represent strong interactions between photons and electrons in the 300–400 nm range [59].

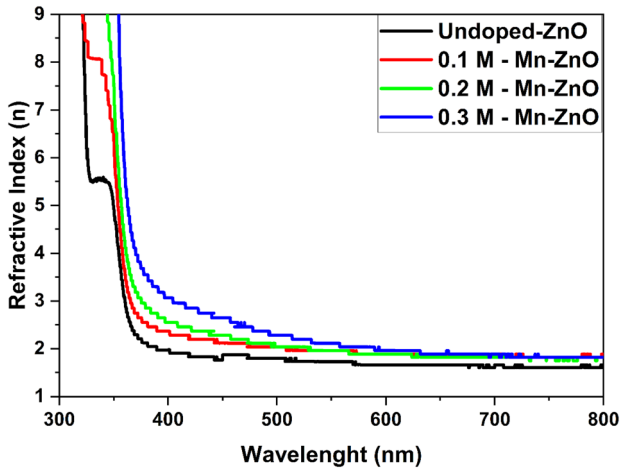


Fig. 7 Refractive index of undoped ZnO and Mn–ZnO thin films

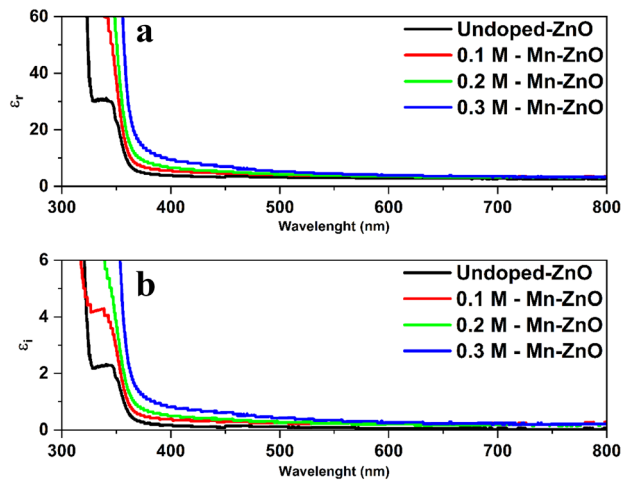


Fig. 8 **a** Real part, **b** imaginary part of dielectric constants versus wavelength of undoped ZnO and Mn–ZnO thin films

3.3 Magnetic and magnetoresistance characteristics

Figure 9 shows the magnetization (M) curves as a function of magnetic field applied (H) between ± 20 kOe at room temperature for undoped ZnO and Mn–ZnO thin films. As seen from the figures, undoped and less (< 0.2 M) doped Mn–ZnO films show predominantly diamagnetic behavior, while more Mn-doped (> 0.2 M) films exhibit an explicit ferromagnetic ordering. As the Mn content increases, the shape of M–H curve changes from diamagnetic to ferromagnetic. The magnetization of Mn-doped (more than 0.2 M) ZnO films tends to increase as the applied field increases. For 0.2 M, the magnetization reaches to the non-expected saturation value in the low magnetic fields (< 5 kOe), while for 0.3 M, the larger fields (> 10 kOe), compared to 0.2 M, are required to obtain the saturation magnetization. Although the presence of the ferromagnetism at RT in some semiconductor oxide nanomaterials including undoped ZnO was reported in previous work [37], some researchers reported the absence of RTFM for undoped and Co-, Mn- and CoMn-doped ZnO materials. Several mechanisms were proposed to explain the origin of the ferromagnetism in DMSs. According to the literature, magnetic cations, free charge carriers and oxygen vacancy defects have been suggested to play an important role on the magnetic origin of oxide DMSs [18, 20, 21, 60]. In our samples, the carrier concentration that is one of the ferromagnetism mechanisms in DMSs increases with

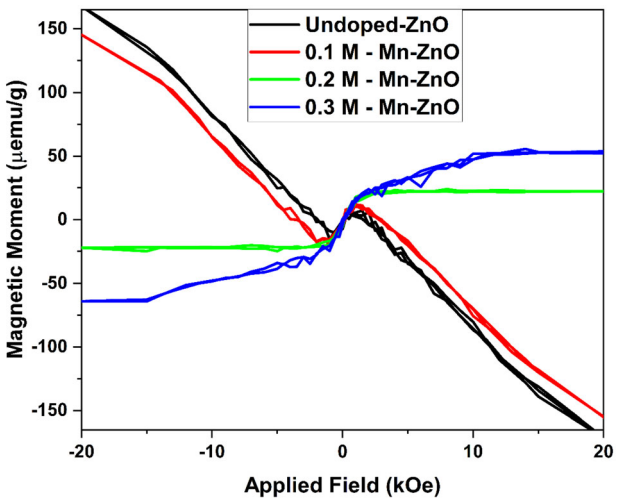


Fig. 9 The magnetization curves of undoped ZnO and Mn–ZnO thin films

increasing Mn dopant (Table 1) and may be a responsible for the ferromagnetic effect. However, it should be known that the exact mechanism of intrinsic ferromagnetism in TM-doped DMSs is still under debate.

In order to support the magnetic behavior findings, we have studied the resistance of the films as a function of the magnetic field. The obtained MR curves are given in Fig. 10. The inset in the figure corresponds to the MR curve of undoped ZnO film. As seen from the inset, for this film, a measurable MR value was not detected up to the maximum magnetic fields (20 kOe) applied in our laboratory, that is, the MR values do not almost vary with increasing magnetic field for both parallel and perpendicular configurations, but there are fluctuations. The similar behavior was also observed for the Mn–ZnO films produced from the solutions with less than 0.2 M. This is an expected result for non-magnetic materials, in which a small change (like 1%) in the resistivity may be observed in very high magnetic fields (like 5–10 tesla). The MR values increase with increasing magnetic field when *H* is both parallel and perpendicular the current (*I*) through the film plane. This effect is known as ordinary magnetoresistance (OMR) [61]. The main figure in Fig. 10 shows the magnetoresistance curves of Mn–ZnO film grown from the solution with 0.3 M Mn. In the figure, the above curve belongs to the longitudinal MR (*H* parallel to *I*) and the bottom curve is for the transverse MR (*H* perpendicular to *I*). As seen from the figure, for 0.3 M, the MR value increases with increasing magnetic field for the parallel configuration (longitudinal—L), while it decreases for the perpendicular configuration (transverse—T). This indicates that the film has an anisotropic magnetoresistance (AMR) effect. In our samples, the shape of the MR curve is similar to the MR curves observed in the Co-doped ZnO films [62, 63] rather than those in ferromagnetic metals such as Ni, Co, Fe and their alloys [32, 64]. For Co-doped ZnO films, the MR becomes negligibly small at the temperatures over 50–100 K and there are only considerable MR values at temperatures below 20 K, while our Mn-doped ZnO films show MR values of about 3% for longitudinal and 5% for transverse measurements at room temperature. It can also be seen that the magnetoresistance of the films does not saturate even in the maximum magnetic fields (± 20 kOe) and there are two peaks on each MR curve as a result of hysteresis, one corresponding to increasing field and the other to decreasing field. The position of these peaks on the MR curves corresponds closely the coercive field on the hysteresis loops. Therefore, it can be concluded that the MR behaviors of the films support their magnetic characteristics.

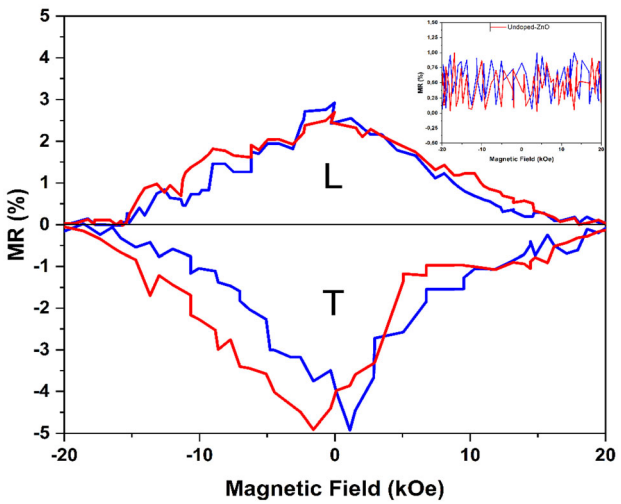


Fig. 10 Magnetoresistance curves of undoped and 0.3 M—Mn–ZnO films. *L* longitudinal, *T* transverse

4 Conclusion

Undoped ZnO and Mn–ZnO films have been prepared sol–gel spin coating method, and their structural, morphological, optical, magnetic and magnetoresistance properties were characterized by XRD, SEM, UV–Vis spectrometer, VSM and HEMS, respectively. It was observed that all films are predominantly crystallized in hexagonal wurtzite ZnO structure and three main peaks from the (101) (100) and (002) planes of the wurtzite structure appear in the XRD patterns as well as other peaks in the larger diffraction angles, but the main peaks are stronger than others. The addition of Mn to ZnO reduces the grain size of the films and increases the carrier concentration. All Mn-doped ZnO films have similar surface morphology that becomes more homogeneous and smooth compared to the surface of undoped ZnO film. The transmittance values of all the films are above 85% in visible region, while they have the absorbance values below 2% in 300–400 nm range. Using the results calculated from UV–Vis measurements, it was found that the band gap of the films decreases with increasing Mn content. Also, the Mn doping rises the refractive index and real and

imaginary values of dielectric constant, compared to those of undoped ZnO films. The VSM measurements showed that undoped ZnO films have a diamagnetic behavior, while the Mn-doped ZnO films show a transition from diamagnetic to ferromagnetic, as the Mn content increases. Furthermore, it was found that the Mn-doped ZnO films have an anisotropic MR value of about 5% and the MR behaviors of the films support their magnetic characteristics. The MR results might be a route to explain the mechanisms that are a responsible for the ferromagnetic effect in DMSs.

Acknowledgments

The authors would like to thank Bursa Technical University for XRD and SEM measurements.

Author contributions

ZG helped in investigation, experimental design, data collection, data analysis, writing—original draft. MA performed investigation, methodology, data analysis, conceptualization, supervision, writing—review and editing. MCH and CA collected the data.

Data availability

The authors declare that all data supporting the findings of this study are available within the article.

Declarations

Conflict of interest The authors declare that there is no conflict of interests regarding the publication of this article.

References

1. M. Yan, M. Lane, C.R. Kannewurf, R.P.H. Chang, Appl. Phys. Lett. **78**, 2342 (2001)
2. A.J. Verkey, A.F. Fort, Thin Solid Films **239**, 211 (1994)
3. M.S. Tokumoto, A. Smith, C.V. Santilli, S.H. Pulcinelli, A.F. Craievich, E. Elkaim, A. Traverse, V. Briois, Thin Solid Films **416**, 284 (2002)
4. K. Matsubara, P. Fons, K. Iwata, A. Yamada, K. Sakurai, H. Tampo, S. Niki, Thin Solid Films **431–432**, 369 (2003)
5. K.L. Chopra, S.R. Das, Thin Film Solar Cells, p. 346. Plenum Press, New York (1983)
6. S. Major, A. Banerjee, K.L. Chopra, Thin Solid Films **143**, 19 (1986)
7. K.L. Chopra, S. Major, D.K. Pandya, Thin Solid Films **102**, 1 (1983)
8. X. Sun, H. Kwork, Optical properties of epitaxially grown zinc oxide films on sapphire by pulsed laser deposition. J. Appl. Phys. **86**, 408–411 (1999). https://doi.org/10.1063/1.370744
9. C.M. Vladut, S. Mihaiu, E. Tenea, S. Preda, J.M. Calderon-Moreno, M. Anastasescu, H. Stroescu, I. Atkinson, M. Gartner, C. Moldovan, M. Zaharescu, Optical and piezoelectric properties of Mn-doped ZnO films deposited by sol–gel and hydrothermal methods. J. Nanomater. (2019). https://doi.org/10.1155/2019/6269145
10. P. Soundarrajan, K. Sethuraman, Interface energy barrier tailoring themorphological structure evolution from ZnO nano/micro rod arrays to microcrystalline thin films by Mn doping. RSC Adv. **5**, 44222–44233 (2015). https://doi.org/10.1039/c5ra06235g
11. M. Willander, O. Nur, Q.X. Zhao, L.L. Yang, M. Lorenz, B.Q. Cao, J.Z. Perez, C. Czekalla, G. Zimmermann, M. Grundmann, Zinc oxide nanorod based photonic devices: recent progress in growth, light emitting diodes and lasers. Nanotechnology **20**(33), 1–40 (2009). https://doi.org/10.1088/0957-4484/20/33/332001
12. A. Raidou, M. Aggour, A. Qachaou, L. Laanab, M. Fahoume, Preparation and characterization of ZnO thin films deposited by Silar method. J. Condens. Mater. **12**(2), 125–130 (2010)
13. H. Kim, A. Piqué, J.S. Horwitz, H. Murata, Z.H. Kafafi, C.M. Gilmore, D.B. Chrisey, Effect of aluminum doping on zinc oxide thin films grown by pulsed laser deposition for organic light-emitting devices. Thin Solid Films **377**(378), 798–802 (2000). https://doi.org/10.1016/S0040-6090(00)01290-6
14. A. LópezSuárez, D. Acosta, C. Magaña, F. Hernández, Optical, structural and electrical properties of ZnO thin films doped with mn. J. Mater. Sci. Mater. Electron. **31**, 7389–7397 (2020). https://doi.org/10.1007/s10854-019-02830-8
15. R.K. Sharma, S. Patel, K.C. Pargaien, Synthesis, characterization and properties of Mn-doped ZnO nanocrystals. Adv. Nat. Sci. Nanosci. Nanotechnol. **3**(3), 1–5 (2012). https://doi.org/10.1088/2043-6262/3/3/035005
16. S. Benramache, A. Arif, O. Belahssen, A. Guettaf, Study on the correlation between crystallite size and optical gap energy of doped ZnO thin film. J. Nanostruct. Chem. **3**, 80 (2013). https://doi.org/10.1186/2193-8865-3-80
17. Z. Ben Ayadi, L. El Mir, K. Djessas, S. Alaya, The properties of aluminum-doped zinc oxide thin films prepared by RF-magnetron sputtering from nanopowder targets. Mater. Sci.

Eng. C **28**(5–6). 613–617 (2008). https://doi.org/10.1016/j.msec.2007.10.006

18. S. Fabbiyola, L. John Kennedy, U. Aruldoss, M. Bououdina, A.A. Dakhel, J. JudithVijaya, Synthesis of co-doped ZnO nanoparticles via co-precipitation: structural, optical and magnetic properties. Powder Technol. **286**, 757–765 (2015). https://doi.org/10.1016/j.powtec.2015.08.054
19. C.B. Fitzgerald, M. Venkatesan, J.G. Lunney, L.S. Dorneles, J.M.D. Coey, Cobalt-doped ZnO—a room temperature dilute magnetic semiconductor. Appl. Surf. Sci **247**, 493–496 (2005). https://doi.org/10.1016/j.apsusc.2005.01.043
20. B. Pal, P.K. Giri, Defect mediated magnetic interaction and high T_C ferromagnetism in Co doped ZnO nanoparticles. J. Nanosci. Nanotechnol. **11**, 1–8 (2011). https://doi.org/10.1166/jnn.2011.4293
21. B. Pal, S. Dhara, P.K. Giri, D. Sarkar, Room temperature ferromagnetism with high magnetic moment and optical properties of Co doped ZnO nanorods synthesized by a solvothermal route. J. Alloys Compd. **615**, 378–385 (2014). https://doi.org/10.1016/j.jallcom.2014.06.087
22. H.-C. You, Y.-H. Lin, Investigation of the sol–gel method on the flexible ZnO device. Int. J. Electrochem. Sci. **7**, 9085–9094 (2012)
23. S. Sharma, C. Periasamy, P. Chakrabarti, Thickness dependent study of RF sputtered ZnO thin films for optoelectronic device applications. Electron. Mater. Lett. **11**, 1093–1101 (2015). https://doi.org/10.1007/s13391-015-4445-y
24. E. Heredia, C. Bojorge, J. Casanova, H. Cánepa, A. Craievich, G. Kellermann, Nanostructured ZnO thin films prepared by sol–gel spin-coating. Appl. Surf. Sci **317**, 19–25 (2014). https://doi.org/10.1016/j.apsusc.2014.08.046
25. S. Balamurali, R. Chandramohan, N. Suriyamurthy, P. Parameswaran, M. Karunakaran, V. Dhanasekaran, T. Mahalingam, Optical and magnetic properties of Mn doped ZnO thin films grown by SILAR method. J. Mater. Sci. Mater. Electron. **24**(6), 1782–1787 (2013). https://doi.org/10.1007/s10854-012-1012-2
26. L. Znaidi, Sol–gel-deposited ZnO thin films: a review. Mater. Sci. Eng. B **174**, 18–30 (2010). https://doi.org/10.1016/j.mseb.2010.07.001
27. S.A. Kamaruddin, K.Y. Chan, H.K. Yow, M.Z. Sahdan, H. Saim, D. Knipp, Zinc oxide films prepared by sol–gel spin coating technique. Appl. Phys. A **104**, 263–268 (2011). https://doi.org/10.1007/s00339-010-6121-2
28. N. Bouchenak Khelladi, N.E. Chabane Sari, Optical properties of ZnO thin film. Adv. Mater. Sci. **13**(1), 21–29 (2013). https://doi.org/10.2478/adms-2013-0003
29. H.-J. Yen, G.-S. Liou, A facile approach towards optically isotropic, colorless, and thermoplastic polyimidothioethers with high refractive index. J. Mater. Chem. **20**, 4080–4084 (2010). https://doi.org/10.1039/c000087f
30. Z. Gültekin, M. Alper, C. Akay, M.C. Hacıismailoğlu, Design and construction of home-made spin coater for OLED production. Int. J. Electron. Device Phys. (2021). https://doi.org/10.35840/2631-5041/1711
31. W. Schwarzacher, D.S. Lashmore, Giant magnetoresistance in electrodeposited films. IEEE Trans. Magn **32**(4), 3133–3153 (1996). https://doi.org/10.1109/20.508379
32. M. Alper, H. Kockar, M. Safak, M.C. Baykul, Comparison of Ni–Cu alloy films electrodeposited at low and high pH levels. J. Alloys Compd. **453**, 1–2 (2008). https://doi.org/10.1016/j.jallcom.2006.11.066
33. C. Peng, J. Guo, W. Yang, C. Shi, M. Liu, Y. Zheng, J. Xu, P. Chen, T. Huang, Y. Yang, Synthesis of three-dimensional flower-like hierarchical ZnO nanostructure and its enhanced acetone gas sensing properties. J. Alloys Compd. **654**, 371–378 (2016). https://doi.org/10.1016/j.jallcom.2015.09.120
34. L. Feng, Z. Xuan, H. Zhao et al., MnO_2 prepared by hydrothermal method and electrochemical performance as anode for lithium-ion battery. Nanoscale Res. Lett. **9**, 290 (2014). https://doi.org/10.1186/1556-276X-9-290
35. A.K.M. Atique Ullah, A.K.M. Fazle Kibria, M. Akter, M.N.I. Khan, A.R.M. Tareq, S.H. Firoz, Oxidative degradation of Methylene Blue using Mn_3O_4 nanoparticles, Water Conserv. Sci. Eng. **1**, 249–256 (2017). https://doi.org/10.1007/s41101-017-0017-3
36. L.V. Stebounova, N.I. Gonzalez-Pech, T.M. Peters, V.H. Grassian, Physicochemical properties of air discharge-generated manganese oxide nanoparticles: comparison to welding fumes. Environ. Sci. Nano **5**, 696–707 (2018). https://doi.org/10.1039/c7en01046j
37. B. Yahmadi, O. Kamoun, B. Alhalaili, S. Alleg, R. Vidu, N.K. Turki, Physical investigations of (Co, Mn) Co-doped ZnO nanocrystalline films. Nanomaterials **10**, 1–13 (2020). https://doi.org/10.3390/nano10081507
38. S. Salam, M. Islam, A. Akram, Sol–gel synthesisof intrinsic and aluminium-doped zinc oxide thinfilms as transparent conducting oxides for thin filmsolar cells. Thin Solid Films **529**, 242–247 (2013). https://doi.org/10.1016/j.tsf.2012.10.079
39. M. Tanemura, P.K. Shishodia, Ferromagnetism in sol–gel derived ZnO:Mn nanocrystalline thin films. Adv. Mater. Lett. **7**(2), 116–122 (2016). https://doi.org/10.5185/amlett.2016.5966
40. S. Yang, Y. Zhang, Structural, optical and magnetic properties of Mn-doped ZnO thin films prepared by sol–gel method. J. Magn. Magn. Mater. **334**, 52–58 (2013). https://doi.org/10.1016/j.jmmm.2013.01.026

41. L. Xu, J. Su, Y. Chen, G. Zheng, S. Pei, T. Sun, J. Wang, M. Lai, Optical and structural properties of ZnO/ZnMgO composite thin films prepared by sol–gel technique. J. Alloys Compd. **548**, 7–12 (2013). https://doi.org/10.1016/j.jallcom.2012.09.011
42. A.K. Zak, M. Abrishami, W. Majid, R. Yousefi, S. Hosseini, Effect of annealing temperature on some structural and optical properties of ZnO nanoparticles prepared by a modified sol–gel combustion methode. Ceram. Int. **37**, 393–398 (2011). https://doi.org/10.1016/j.ceramint.2010.08.017
43. A.R. Ansari, S. Hussain, M. Imran, A. Al-Ghamdi, M.R. Chandan, Optical investigations of microwave induced synthesis of zinc oxide thin-film. Mater. Sci. (Poland) **36**(2), 304–309 (2018). https://doi.org/10.1515/msp-2018-0041
44. C. Aydın, The dispersion energy parameters, linear and nonlinear optical properties of transparent mn:ZnO nanolayers. Eur. Mech. Sci. **4**(2), 82–89 (2020). https://doi.org/10.26701/ems.710165
45. S. Sharma, C. Periasamy, P. Chakrabarti, Thickness dependent study of RF sputtered ZnO thin films for optoelectronic device applications. Electron. Mater. Lett. **11**(6), 1093–1101 (2015). https://doi.org/10.1007/s13391-015-4445-y
46. Z.N. Kayani, I. Shah, B. Zulfiqar, S. Riaz, S. Naseem, A. Sabah, Structural, optical and magnetic properties of nanocrystalline co-doped ZnO thin films grown by sol–gel. Z. Nat. **73**(1a), 13–21 (2018). https://doi.org/10.1515/zna-2017-0302
47. L. Wei, G. Wang, C. Chen, J. Liao, Z. Li, Enhanced visible light photocatalytic activity of ZnO nanowires doped with Mn^{2+} and Co^{2+} ions. Nanomaterials **19** 7, 1–11 (2017). https://doi.org/10.3390/nano7010020
48. V.K. Verma, N.K. Pandey, MnO_2-ZnO hexagonal nanomaterials: characterization and high performance humidity sensing application. IJSRPAS **6**, 69–79 (2018). https://doi.org/10.26438/ijsrpas/v6i6.6979
49. Y. Wang, X. Hao, Z. Wang, M. Dong, L. Cui, Facile fabrication of Mn^{2+} doped ZnO photocatalysts by electrospinning. R. Soc. Open. Sci. **7**, 191050–191057 (2020). https://doi.org/10.1098/rsos.191050
50. H.A. Khawal, U.P. Gawai, K. Asokan, B.N. Dole, Modified structural, surface morphological and optical studies of Li^{3+} swift heavy ion irradiation on zinc oxide nanoparticles. RSV Adv. **6**, 49068–49075 (2016). https://doi.org/10.1039/C6RA04803J
51. K. Dhanshree, T. Elangovan, Synthesis and characterization of ZnO and Mn-doped nanoparticles. IJSR **4**(11), 1816–1820 (2015). https://doi.org/10.21275/v4i11.nov151529
52. O. Bilgili, The effect of Mn doping on the structural and optical properties of ZnO. Acta Phys. Pol. **136**, 460–466 (2019). https://doi.org/10.12693/APhysPolA.136.460
53. S. Roguai, A. Djelloul, C. Nouveau, T. Souier, A.A. Dakhel, M. Bououdina, Structure, microstructure and determination of optical constants from transmittance data of co-doped $Zn_{0.90}$ $Co_{0.05}$ $M_{0.05}$ O (M = Al, Cu, Cd, Na) films. J. Alloys Compd. **599**, 150–158 (2014). https://doi.org/10.1016/j.jallcom.2014.02.080
54. Q.M. Al-Bataineh, M. Telfah, A.A. Ahmad, A.M. Alsaad, I.A. Qattan, H. Baaziz, Z. Charifi, A. Telfah, Synthesis, crystallography, microstructure, crystal defects, optical and optoelectronic properties of ZnO:CeO_2 mixed oxide thin films. Photonics **7**(112), 1–19 (2020). https://doi.org/10.3390/photonics7040112
55. A.S. Hassanien, Studies on dielectric properties, opto-electrical parameters and electronic polarizability of thermally evaporated amorphous $Cd_{50}S_{50-x}Se_x$ thin films. J. Alloys Compd. **671**, 566–578 (2016). https://doi.org/10.1016/j.jallcom.2016.02.126
56. A.M. Alsaad, Q.M. Al-Bataineh, A.A. Ahmad, Z. Albataineh, A. Telfah, Optical band gap and refractive index dispersion parameters of boron-doped ZnO thin films: a novel derived mathematical model from the experimental transmission spectra. Optik **211**, 164641–164653 (2020). https://doi.org/10.1016/j.ijleo.2020.164641
57. B. Mehmood, M.I. Khan, M. Iqbal, A. Mahmood, W. Al-Masry, Structural and optical properties of Ti and Cu co-doped ZnO thin films for photovoltaic applications of dye sensitized solar cells. Int. J. Energy Res. **45 2**, 1–15 (2020). https://doi.org/10.1002/er.5939
58. A. Boukhachem, B. Ouni, M. Karyaoui, A. Madani, R. Chtourou, M. Amlouk, Structural, opto-thermal and electrical properties of ZnO:Mo sprayed thin films. Mater. Sci. Semicond. Process. **15**(3), 282–292 (2012). https://doi.org/10.1016/j.mssp.2012.02.014
59. M.M. A.Gadallah, El-Nahass, Structural, optical constants and photoluminescence of ZnO thin films grown by sol–gel spin coating, Adv. Condens. Matter Phys. **2013**, 1–11 (2013). https://doi.org/10.1155/2013/234546
60. X.L. Wang, K.H. Lai, A. Ruotolo, A comparative study on the ferromagnetic properties of undoped and Mn-doped ZnO. J. Alloys Compd. **542**, 147–150 (2012). https://doi.org/10.1016/j.jallcom.2012.07.035
61. C.L. Chien, J.Q. Xiao, J.S. Jiang, Giant negative magnetoresistance in granular ferromagnetic systems (invited). J. Appl. Phys. **73**, 5309 (1993). https://doi.org/10.1063/1.353765
62. P. Stamenov, M. Venkatesan, L.S. Dorneles, D. Maude, J.M.D. Coey, Magnetoresistance of Co-doped ZnO thin films. J. Appl. Phys. **99**, 08M124 (2006). https://doi.org/10.1063/1.2172194

63. S. Venkatesh, A. Baras, J.-S. Lee, I.S. Roqan, The magnetic ordering in high magnetoresistance Mn-doped ZnO thin films. AIP Adv. **6**, 035019 (2016). https://doi.org/10.1063/1.4944954
64. T.R. McGuire, R.I. Potter, Anisotropic magnetoresistance in ferromagnetic 3D allyos. IEEE Trans. Magn. (MAG-11) (1975). https://doi.org/10.1109/TMAG.1975.1058782

Publisher's Note Springer Nature remains neutral with regard to jurisdictional claims in published maps and institutional affiliations.

Springer Nature or its licensor (e.g. a society or other partner) holds exclusive rights to this article under a publishing agreement with the author(s) or other rightsholder(s); author self-archiving of the accepted manuscript version of this article is solely governed by the terms of such publishing agreement and applicable law.